magnetochemistry

MDPI

Article

Exploring Crystal Structure, Hyperfine Parameters, and Magnetocaloric Effect in Iron-Rich Intermetallic Alloy with $ThMn_{12}$-Type Structure: A Comprehensive Investigation Using Experimental and DFT Calculation

Jihed Horcheni [1,2,*], Hamdi Jaballah [1], Essebti Dhahri [2] and Lotfi Bessais [1]

[1] CNRS, ICMPE, University Paris Est Creteil, UMR 7182, 2 Rue Henri Dunant, F-94320 Thiais, France ; hamdi.jaballah@cnrs.fr (H.J.); lotfi.bessais@cnrs.fr (L.B.)
[2] Laboratoire de Physique Appliquée, Faculté des Sciences, Université de Sfax, Sfax 3000, Tunisia; essebti.dhahri@fss.usf.tn
* Correspondence: jihed.horcheni@cnrs.fr

Abstract: In this study, we give a thorough evaluation of the structural, magnetic, and magnetocaloric properties in iron-rich $PrFe_{11}Ti$ intermetallic alloy with $ThMn_{12}$-type structure using a combination of experimental and theoretical analysis. X-ray diffraction coupled with Rietveld refinement was used to characterize the structure, which revealed a unique tetragonal crystal structure with $I4/mmm$ space group. The 8*i* site was identified as the preferred site for the Ti atom. This finding was confirmed by various techniques, including XRD, DFT, and Mössbauer spectrometry. Magnetic properties were studied through intrinsic magnetic measurements and magnetocaloric effect analysis. Mössbauer spectroscopy was employed to probe the local magnetic environment and for further characterization of the material's magnetic properties. The experimental results were complemented by theoretical calculations based on density functional theory (DFT). A promising magnetocaloric effect is observed, with a significant maximum magnetic entropy ($-\Delta S_M^{max} = 2.5\ J{\cdot}kg^{-1}{\cdot}K^{-1}$) and a relative cooling power about 70 $J{\cdot}kg^{-1}$ under low magnetic field change $\mu_0\Delta H = 1.5$ T. Overall, our results provide a deeper understanding of the structural and magnetic properties of the material under study and demonstrate the effectiveness of the combined experimental and theoretical approach in the investigation of complex materials. The insights gained from this study could have implications for the development of advanced magnetic materials with enhanced properties for potential magnetic applications.

Keywords: magnetic materials; intermetallic compounds; Mössbauer; electronic structure; magnetocaloric effect

Citation: Horcheni, J.; Jaballah, H.; Dhahri, E.; Bessais, L. Exploring Crystal Structure, Hyperfine Parameters, and Magnetocaloric Effect in Iron-Rich Intermetallic Alloy with $ThMn_{12}$-Type Structure: A Comprehensive Investigation Using Experimental and DFT Calculation. *Magnetochemistry* **2023**, *9*, 230. https://doi.org/10.3390/magnetochemistry9110230

Academic Editor: Andrea Caneschi

Received: 9 September 2023
Revised: 31 October 2023
Accepted: 9 November 2023
Published: 18 November 2023

1. Introduction

Iron-rich ternary compounds with a tetragonal $ThMn_{12}$ structure have piqued the curiosity of researchers looking for high-performance magnetic materials for a variety of applications. Unlike the binary compounds RFe_{12} (where R denotes rare earth elements), which prove to be unstable [1], it is necessary to incorporate a stabilizing element such as a transition metal (Cr, V, Ti, V, Mo, W, Mn) [2,3] or Si and Al [4,5] to obtain the $ThMn_{12}$ phase. However, this modification of the crystalline structure has significant effects on the magnetic properties of these materials, leading to a dilution of the magnetization and a reduction in the Curie temperatures. Notwithstanding these obstacles, this category of materials has been extensively studied and deemed as the most significant in recent times due to its cost-effectiveness. It comprises only 7% of the rare earth, exhibits a remarkable magnetic moment, and exhibits significant magnetocrystalline anisotropy, which is crucial for permanent magnet applications. Right now, most research is focused on using permanent magnets and magnetic recording devices [6–8]. Recently, a new avenue has emerged in the

form of magnetic refrigeration, which is an environmentally friendly technology that shows great promise in achieving high energy conversion efficiency [9]. Central to its applications is the magnetocaloric effect (MCE), where a change in the applied magnetic field ($\mu_0\Delta H$) leads to a reversible temperature change. Scientists have identified cutting-edge magnetic materials with high magnetic entropy and a large shift in magnetization at the magnetic phase transition temperature. These materials also have a high relative cooling power (RCP), which indicates their capacity to transport heat efficiently between hot and cold reservoirs throughout an optimal thermodynamic cycle [10]. Examples include Mn–As-based materials [11], La–Fe–Si alloys [12], as well as Fe–Rh compounds [13] and R–MnO manganites [14–16]. Additionally, $R_2(Fe, X)_{17}$ (R = Pr, Sm, Er, Gd, Ce, Nd and X = Ni, Co, Cu, Mn, Al, Si. . .) [17–22] compounds have undergone extensive study over the past two decades, all with the overarching goal of improving both the magnitude and temperature range of MCE. Materials with $ThMn_{12}$-type structure such as $Nd(Fe, Mo)_{12}$, which have a maximum value of the change of magnetic entropy at $\mu_0\Delta H = 5$ T ($-\Delta S_M^{max}$=2.38 J·kg^{-1}·K^{-1}) [23], $R(Fe, X)_{12}$ (R = Nd, Sm and X = Ti, V) ($-\Delta S_M^{max}$ = 1.6 J·kg^{-1}·K^{-1} at $\mu_0\Delta H = 1.5$ T) [24], $Gd(Fe, Cr)_{12}$ ($-\Delta S_M^{max}$=1.82 J·kg^{-1}·K^{-1}, and RCP = 10.5 J·kg^{-1} at $\mu_0\Delta H = 1.5$ T) [25], and $Er(Fe, Mn)_{12}$ ($-\Delta S_M^{max}$ = 1.92 J·kg^{-1}·K^{-1} at $\mu_0\Delta H = 5$ T) [26], have already demonstrated promising magnetocaloric properties, showcasing their potential for high-temperature magnetic refrigeration applications. However, among these high-performing compounds, $PrFe_{11}Ti$ stands out due to its exceptional magnetization and the absence of magnetic hysteresis around the magnetic transition temperature, which represents the operating temperature of magnetocaloric materials. Interestingly, despite its magnetic promise, there has been a surprising lack of research exploring the magnetocaloric effects of $PrFe_{11}Ti$, a gap that our study aims to fill.

In this study, our main objective is to evaluate the magnetocaloric effect (MCE) in $PrFe_{12}Ti$. This study combines experimental approaches such as Mössbauer spectroscopy and magnetization measurements with theoretical calculations based on density functional theory. By employing this integrated approach, we aim to predict and elucidate the material's magnetic and electronic properties, as well as identify the preferential site of titanium incorporation. This insight will significantly enhance our understanding of its potential for magnetic applications.

2. Experimental Techniques

By arc melting in an inert argon environment, an alloy with nominal compositions of $PrFe_11Ti$ was created with high-purity components of Pr 99.98%, Fe 99.99%, and Ti 99.99%. The sample was turned and remelted five times in order to ensure appropriate homogeneity, with an excess of 12% Pr to compensate for any Pr losses owing to evaporation. After melting, the ingot was covered in tantalum foil and sealed in a quartz tube under a vacuum of 2×10^{-6} bar before being annealed at 1150 °C for 1 week to achieve adequate homogeneity. Following the heat treatment, the structure was automatically quenched with water to freeze it at the annealing temperature. The PFT sample was finally hand-crushed into fine powder, which was then sieved using a metal sieve to make the measurements.

The final compound's quality and phase purity were verified at room temperature using X-ray-diffraction patterns (XRD) performed on a Bruker D8 diffractometer with Cu–Kα radiation $\lambda = 1.5405$. The XRD data of the sample were acquired at room temperature between $2\theta = 10°$ and $2\theta = 90°$ with a step width of 0.02 and counting times of 6 s per point. The Rietveld method, which has been implemented in the FullProf program, was used to refine the pattern [27,28]. Magnetic property measurements were assessed at varying temperature regimes employing two magnetic measurement devices. Specifically, low-temperature measurements were conducted using a Quantum Design Physical Properties Measurement System (PPMS), employing external applied magnetic fields (H_a) spanning from 0 to 9 Tesla. High-temperature assessments were carried out utilizing a DSM-8 MANICS differential magnetometer, with H_a values extending from 0 to 1.55 Tesla. The Curie temperature (T_C) was ascertained by analyzing the temperature dependency of

magnetization curves, denoted as $M(T)$, within the temperature range of 5 to 650 Kelvin, while applying a magnetic field of $\mu_0 H_a$ = 0.13 T.

Additionally, measurements of the magnetic-field dependence of the magnetization curves, $M(H)$, have been realized. Between two successive isothermal $M(H)$ curves, there was a temperature step of 5 K close to T_C and 10 K far from the magnetic ordering temperature. The data were collected at each temperature with constant DC-applied magnetic field steps of $\mu_0 H = 0.09$ T in the magnetic field range between 0 and 1.55 T.

Mössbauer spectra were obtained using a Wissel constant-acceleration spectrometer equipped with a 25 mCi Cobalt-57 source embedded in a rhodium (Rh) matrix, which was calibrated at room temperature with α-Fe foil. For the preparation of Mössbauer absorbers, powder samples of $PrFe_{11}Ti$ were used, yielding absorbers with a thickness of 10 mg/cm^2. Isomeric displacements δ and quadrupole effects 2ϵ are estimated with an error of $\pm$0.01 mm/s. Hyperfine fields are estimated with an error of $\pm$0.1 T. The collected spectra underwent analysis through least-squares fitting, following the procedure outlined in Refs. [29,30].

3. Results and Discussion

3.1. Crystal Structure

In compounds of the RT_5 series, where R represents rare earth and T denotes transition metal, possessing the $CaCu_5$ type crystalline structure and hexagonal symmetry in the *P6/mmm* space group, the R ions are located at the 1*a* site (0, 0, 0), while the T ions are distributed across two distinct sites: 2*c* (1/3, 2/3, 0) and 3*g* (1/2, 0, 1/2) (refer to Figure 1). This structure can also be described as a stack of layers of two types. Every second layer is made up of R atoms in the center of the hexagons formed by the T atoms, while the second layer consists only of hexagons formed by the T atoms. This structure can evolve into non-stoichiometric structures.

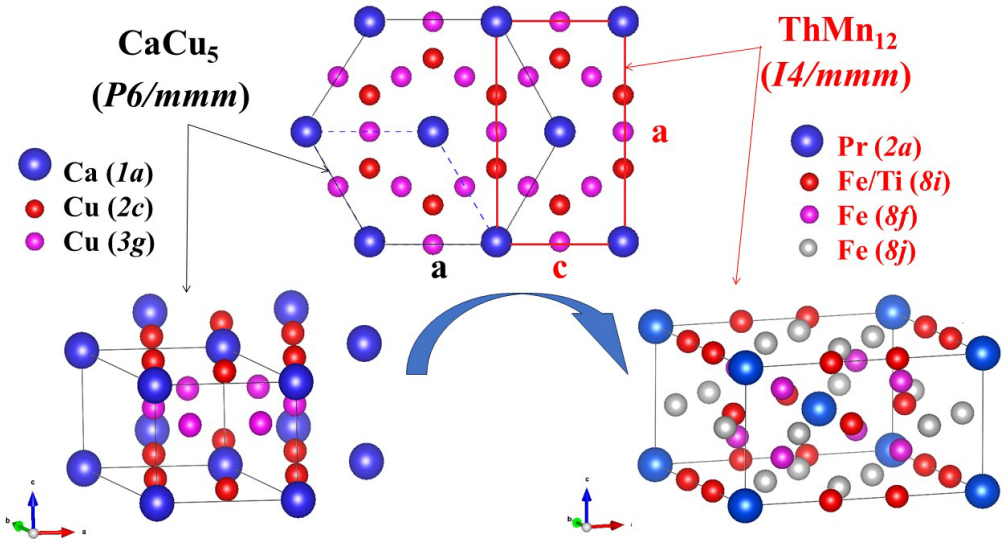

Figure 1. The crystal structure of the hexagonal $CaCu_5$ phase (on the left with black color) and the tetragonal $ThMn_{12}$ phase (on the right with red color). In the middle is the relationship between the two structures.

According to the structural model proposed by Givord et al. ($R_{1-s}T_{2s+5}$) [31], which suggests a narrowing of the hexagons formed by the metal atoms as a result of a disordered substitution of s rare earth atoms by s pairs of metal atoms (T–T dumbbells): atomic ordering in the 1/5 composition phase generates equilibrium phases of composition 2/17 (s = 0.33), 3/29 (s = 0.4), and 1/12 (s = 0.5). In the case of the 1/12 composition phase, the

ordered substitution of 1/2 atom of R (s = 0.5) produces the alloy RT_{12} with a tetragonal $I4/mmm$ structure:

$$2(RT_5) - R + 2(T, dumbbell) \longmapsto RT_{12}.$$

A representation of the tetragonal cell is given in Figure 1. The 24 T atoms in the lattice are distributed over the three sites 8*i* (x, 0, 0), 8*j* (x, 0.5, 0), and 8*f* (1/4, 1/4, 1/4) while the rare earth atoms R occupy site 2*a*. One can see in the middle of Figure 1 that the lattice parameters of the $I4/mmm$ and $P6/mmm$ ($CaCu_5$) structures are related by $a(CaCu_5) = c(ThMn_{12})$ and $c(CaCu_5) = 1/2\ a(ThMn_{12})$. However, in the latter case, a third element is required to stabilize the structure. It has previously been shown that for $R(Fe, T)_{12}$ (where R = Y, Nd, Sm, Pr, Ce and T = Zr, Cr, Mo, V, Ti) [2,3,32,33], substitution atoms preferentially occupy site 8*i* rather than 8*j* and 8*f*. In order to determine the most suitable location for the Titanium atom, a systematic Rietveld refinement was carried out. This involved adjusting the placement of Ti in the four different crystallographic sites denoted as 8*i*, 8*j*, and 8*f* using Wyckoff notation. The subsequent step involved evaluating the corresponding reliability factor (R_B) for each configuration. The results obtained indicate that the 8*i* site displayed the lowest R_B value, suggesting it may be the most favorable position and therefore the preferred site for Ti.

Refined X-ray diffraction patterns at room temperature depicted in Figure 2 show that the PFT 1:12 sample is well crystallized in a single phase without any detectable foreign impurities (α-Fe) due to praseodymium excess added in order to compensate the evaporation losses, and the peak reflections are well indexed into tetragonal symmetry $ThMn_{12}$-type structure with $I4/mmm$ space group. The obtained unit cell parameters, the atomic positions, R_B, and χ^2 factors from the best refinement of our compound are presented in Table 1. The cell parameters and atomic positions obtained are in concordance with those found for $Pr(Fe, M)_{12}$ alloys (M = Mo, Ti, V) [30,34,35].

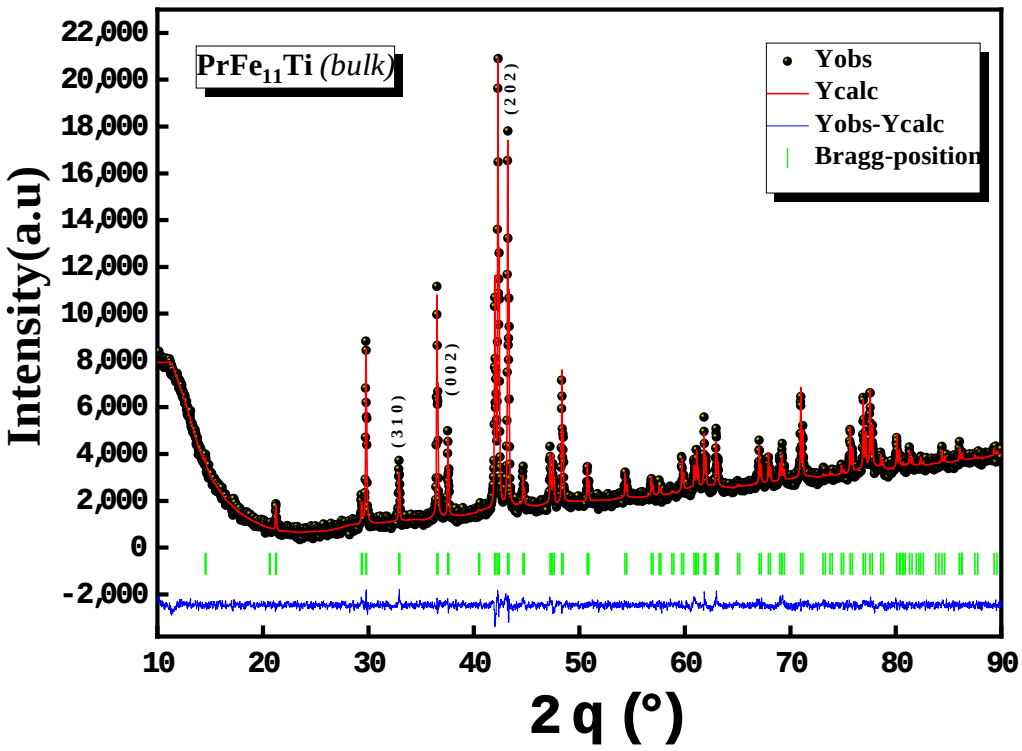

Figure 2. Refined X-ray diffraction patterns of PFT compound at ambient temperature. The emergence of superstructure reflection peaks denoted by hkl (202), (002), (202) are indicative of the $ThMn_{12}$-type structure $I4/mmm$.

Table 1. Crystallographic parameters from Rietveld refinement of $PrFe_{11}Ti$: a and c are unit cell parameters, (x, y, z) are the atomic position, and χ^2, R_B are agreement factors.

Sample		**$PrFe_{11}Ti$**		
Space group		$I4/mmm$		
Cell parameters		$a = b$ (Å)	8.601(1)	
		c (Å)	4.789(1)	
		c/a	0.556	
		V (Å^3)	354.308(1)	
Atom site	x	y	z	Atomic number
Pr(2a)	0	0	0.344(1)	2
Fe/Ti(8i)	0.360(1)	0	0	6/2
Fe(8j)	0.274(1)	0.5	0	8
Fe(8f)	0.25	0.25	0.25	8
Agreement	R_B	6.17		
factors	R_F	7.5		
	χ^2	1.40		

3.2. Intrinsic Magnetic Properties

In this section, we investigate the magnetization (M) of the $PrFe_{11}Ti$ combination as a function of temperature (T). Because of its peculiar magnetic characteristics, understanding the magnetic behavior of $PrFe_{11}Ti$ across a wide temperature range is critical. The Curie temperature (T_C) of $PrFe_{11}Ti$, which indicates the transition from ferromagnetic to paramagnetic behavior, is one of the primary goals of this research. We may establish the critical temperature at which this transition happens by carefully monitoring M as T changes, revealing insight into the underlying magnetic interactions in our compound. Moreover, we will assess our results with those obtained from analogous compounds, providing crucial insights into the magnetic properties of $PrFe_{11}Ti$. This comparative analysis promises not only to enhance our comprehension of the material's magnetic behavior but also to contribute to the broader domain of magnetic materials research. By discerning how $PrFe_{11}Ti$ stacks up against other compounds concerning T_C and magnetic susceptibility, we can gain deeper insights into the underlying mechanisms governing its distinct magnetic attributes. This, in turn, may open avenues for the development of novel materials with tailored magnetic functionalities. The temperature dependence of the magnetization data $M(T)$ obtained at a magnetic field of 0.13 T for the PFT bulk sample is shown in Figure 3. The magnetization is remarkably stable as the temperature rises in the ferromagnetic state; however, when the temperature reaches a particular value, we see a dramatic reduction in the magnetization value, which is an indication of the transition from the ferromagnetic to the paramagnetic state. The drop in magnetization value transpires over a moderately extensive temperature span, approximately ∼30 K, signifying a transition of second-order. The examination of the phase transition's characteristics will be studied in more detail later in subsequent sections. A transition from ferromagnetic to paramagnetic states (FM–PM) takes place at T_C = 543 K, as ascertained from the minimum of dM/dT (refer to the inset of Figure 3).

Table 2 presents in this paper the Curie temperature values for $PrFe_{11}Ti$ alongside other $RFe_{11}Ti$ compounds, facilitating a comparative analysis. A notable observation from Table 2 is the significant impact of the type of rare earth atom on T_C values, especially when contrasting (Y, Pr, Nd)$Fe_{11}Ti$ with (Sm, Gd)$Fe_{11}Ti$. Interestingly, despite the close atomic radii of Sm, Pr, and Nd, which imply similar cell volumes and interatomic distances, there is a substantial, ∼50 K, difference in T_C between $PrFe_{11}Ti$ and $SmFe_{11}Ti$, among others. Another example of comparison is the atomic radius of Gd (180 pm), which is smaller than the atomic radius of Pr and Nd (185 pm). If we consider only the magnetovolume effect, one would expect a lower Curie temperature (T_C) for ($GdFe_{11}Ti$) compared to (Pr, Nd)$Fe_{11}Ti$. However, this is not the case. These findings strongly suggest that electronic

effects play a pivotal role in determining Curie temperature, thus indicating the dominance of electronic effects over the magnetovolume effect in these systems.

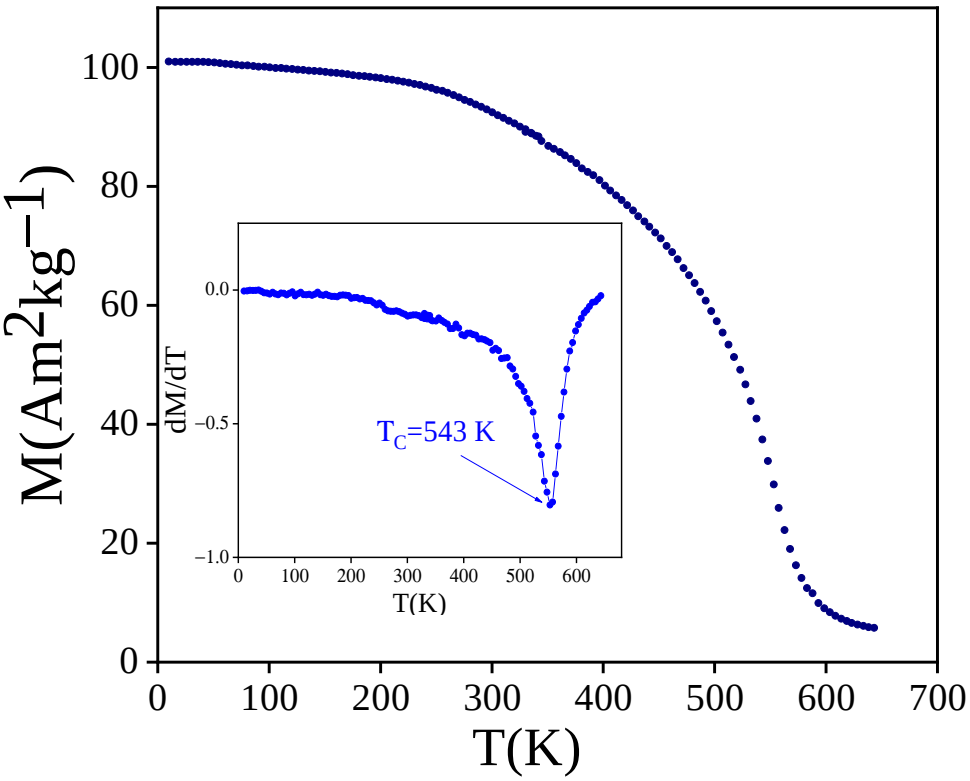

Figure 3. Variation of the magnetization as a function of temperature at 0.13 T of the PFT alloy. The inset is the plot of dM/dT versus T.

Table 2. T_C of some $RFe_{11}Ti$ compounds.

Compound	T_C (K)	Ref.
$YFe_{11}Ti$	525	[36]
$PrFe_{11}Ti$	547	[30]
$PrFe_{11}Ti$	543	This work
$NdFe_{11}Ti$	552	[24]
$SmFe_{11}Ti$	589	[37]
$GdFe_{11}Ti$	604	[25]

The magnetization of $PrFe_{11}Ti$ compound was measured at a temperature of 10 K, and the findings are shown in Figure 4. The "law of approach to saturation" was used to calculate the saturation magnetization value [38]:

$$M = M_S \times \left(1 - \frac{a}{H^2}\right) \quad \text{with} \quad a = \frac{8}{105} \times \left(\frac{K}{M_S}\right)^2 \tag{1}$$

where K is the anisotropy constant. We can further determine the magnetocrystalline anisotropy constant K for our compound. The determined M_S and K are about 22.72 μ_B and 4.57 MJ/m^3, respectively, at T = 10 K. Using K and saturation magnetization M_S, we can deduce the anisotropy field H_A with the following equation:

$$H_A = \frac{2 \times K}{M_S} \tag{2}$$

We found that $\mu_0 H_A$ = 5.8 T. Furthermore, we derived iron magnetic moments per formula unit (μ_{Fe}) from measurements of low-temperature saturation magnetization. The

specific value for $PrFe_{11}Ti$ is 2.06 $\mu_B/f.u$. In the next phase of our investigation, we will subject this determination to a comparative analysis with findings derived from Mössbauer spectra and DFT calculations.

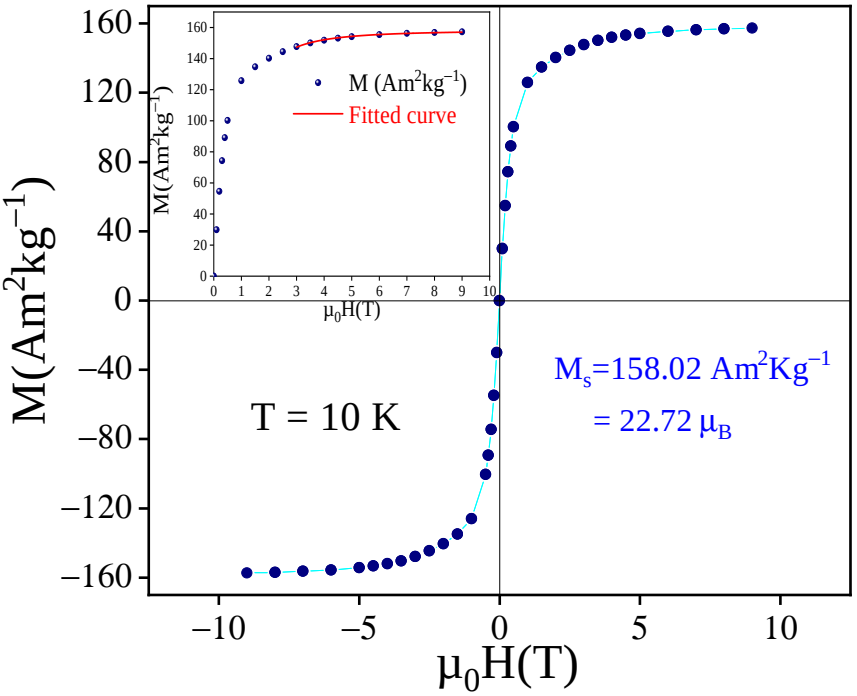

Figure 4. Magnetization $M(H)$ vs. magnetic field of $PrFe_{11}Ti$ measured at T = 10 K. The red line represents the fitted curve with the law of approach to saturation.

3.3. Mössbauer Spectrometry and DFT Calculations

In order to elucidate the ferromagnetic properties of $PrFe_{11}Ti$ compounds belonging to the fascinating family of $ThMn_{12}$ phases, we probed the Mössbauer spectra in detail. The Mössbauer spectra of PFT in the $ThMn_{12}$-type phase at a temperature of 10 K are presented in Figure 5. Through scrutiny of this substance at both low temperature (T = 10 K) and elevated temperature ($T = K$), we unearthed discernible spectral configurations, manifesting as clearly defined sextuplets. These findings constitute robust proof of the material's ferromagnetic nature. The plot thickens when we delve into the source of this complexity, attributed to the coexistence of three non-equivalent crystallographic sites and interactions between iron atoms and Pr vacancies at site 8j.The collected spectra underwent a thorough analysis through the least squares adjustment method, following the procedure outlined in Refs. [29,30]. This strategy hinges on two pivotal prerequisites. Firstly, it entails allocating hyperfine parameter assortments to distinct sextets, predicated on the interrelation between the volumes of Wigner–Seitz cells (WSC) and the corresponding isomeric shift. Consequently, a greater WSC volume leads to a more significant isomeric shift. Additionally, it considers the potential substitution of Fe by Ti at the $8i/8j/8f$ site within the $ThMn_{12}$ structure. This analysis enables the calculation of the abundance distribution of the sextet across the three distinct iron ($8i/8j/8f$) sub-sites, employing a multinomial distribution law.

Based on the crystallographic insights provided in Table 1, and factoring in the respective atomic radii of Pr, Fe, and Ti (1.82, 1.26, and 1.47), we computed the Wigner–Seitz cell (WSC) volumes, as outlined in Table 3. This computation was executed by employing Dirichlet domains and coordination polyhedra unique to each distinct crystallographic site. We notably discerned that site 8i holds the most substantial Wigner–Seitz cell volume, signifying its favored position for hosting titanium atoms. This aligns with the larger atomic radius of titanium when compared to iron. The refined average hyperfine parameters have been collated and are presented in Table 3. The sequence of hyperfine fields, denoted as $H_{HF}\{8i\} > H_{HF}\{8j\} > H_{HF}\{8f\}$, has been derived. Importantly, it is worth highlight-

ing that the sequence of the refined average isomer shift corresponds to the sequence of WSC volumes. This correspondence strongly validates our initial assumption (Rietveld refinement). To deduce the average magnetic moment of iron $\langle \mu_{Fe} \rangle$ from the weighted average hyperfine field $\langle H_{HF} \rangle$ [39], a convenient conversion factor of 15.6 T/μ_B can be utilized with reasonable approximation. For the $PrFe_{11}Ti$ compound at $T = 10$ K, we have determined $\mu_0 \langle H_{HF} \rangle$ = 28.5 T, corresponding to $\langle \mu_{Fe} \rangle = 1.82\ \mu_B$.

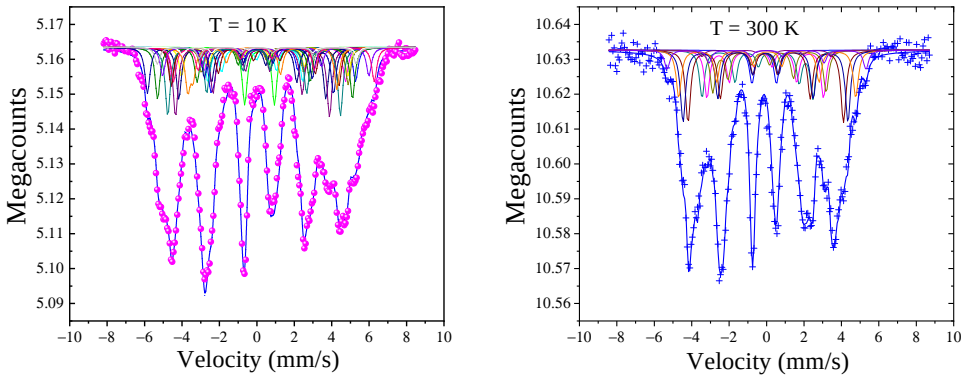

Figure 5. Mössbauer spectrum of PFT at $T = 10$ K (**left**) and 300 K (**right**). The magenta dots and the blue symbol represent the experimental data selected at 10 K and 300 K, respectively. The solid blue line represents the fit, and the solid colored lines represent the nine sextets utilized in the fitting process.

Table 3. Wigner–Seitz cell volume (WSCV) and Mössbauer hyperfine parameters for $PrFe_{11}Ti$: hyperfine field (H_{HF}), isomer shift (δ), and quadrupole interaction (2ε). $\langle HF \rangle$ denotes the average of the hyperfine parameters.

	$\mu_0 H_{HF}$ (T)		δ (mm/s)		2ε (mm/s)		WSCV (Å^3)
T(K)	10	300	10	300	10	300	-
Fe{8*i*}	31.2	27.1	0.08	−0.08	0.13	0.09	13.1
Fe{8*j*}	28.7	23.8	0.01	−0.10	0.11	0.09	11.6
Fe{8*f*}	26.3	21.8	−0.01	−0.12	0.06	0.04	10.6
Pr{2*a*}	-	-	-	-	-	-	23.3
$\langle HF \rangle$	28.5	24.2	0.03	−0.09	0.10	0.08	-

We employed band structure calculations to calculate the total energy as well as to describe the magnetic configuration of the PFT compound. We used the full potential linearized augmented plane wave (FP-LAPW) method [40] to solve the Kohn–Sham equations [41] within the framework of density functional theory (DFT). These calculations were carried out using the WIEN2k code [42], and we utilized the generalized gradient approximation (GGA) with the full Perdew–Burke–Ernzerhof (PBE) correlation energy [43]. In our computations, we used the following steps:

- The cut-off parameter was established as $R_{MT} \times K_{max}$ =7, where K_{max} denotes the magnitude of the largest K vector.
- We implemented G_{max} = 12 $Ry^{1/2}$ for Fourier potential expansion.
- 1200 k-points in the Brillouin zone.
- The muffin-tin radii R_{MT} were set at 2.50, 2.14, and 2.17 Bohr for Pr, Fe, and Ti atoms, respectively.
- To distinguish between valence and core states, we adopted a cut-off energy of $E = 7$ Ry
- Convergence was deemed achieved when the total energy difference was less than 10^{-4} Ry and the charge was below 10^{-4} electron charges.

Our band structure calculations took into account a spin-polarized potential to accommodate the ferromagnetic state of the PFT compound alongside the total density of states (DOS). According to these calculations, we find typical metallic behavior in both the

spin-up and spin-down components. This effect is clearly shown in Figure 6. The density of state (DOS) structure exhibits a qualitative resemblance to the DOS of ferromagnetic elemental iron in its body-centered cubic (bcc) structure [44].

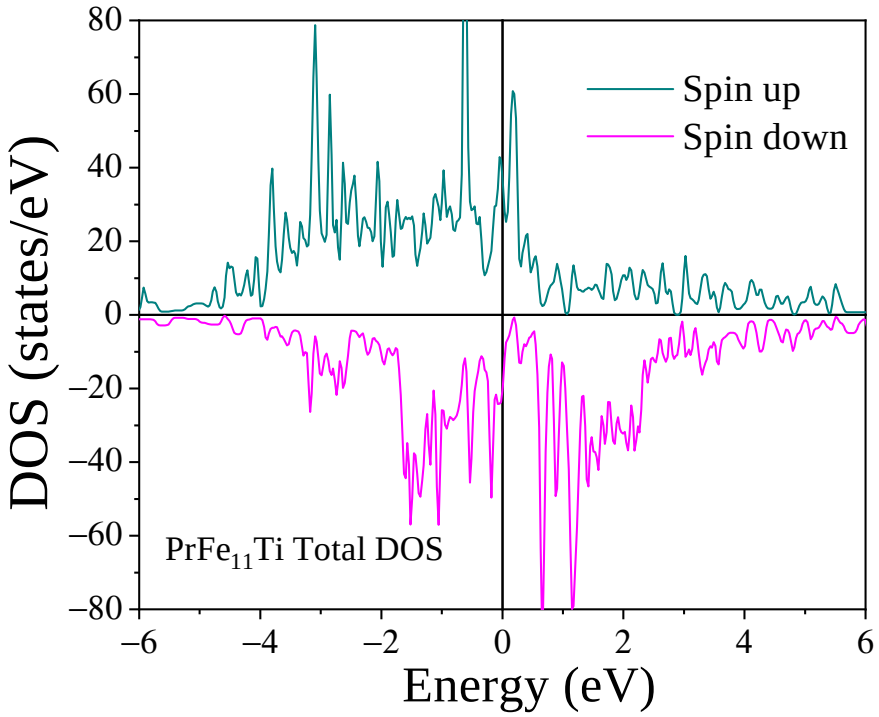

Figure 6. Total densities of states for PFT intermetallic compound.

The partial density of states analysis of the $PrFe_{11}Ti$ intermetallic compound, as shown in Figure 7, highlights a significant impact from the iron sublattices on the density of states near the Fermi level (E_F). This influence can be chiefly attributed to the contribution of $3d$ states originating from the iron atoms. Furthermore, a noteworthy observation is made regarding the $4f$ states of Pr. The $4f$ states, governing the behavior of the electrons in the Pr atom, exhibit a distinct difference based on their spin orientations. Specifically, those with majority spins are partially occupied, indicating a degree of electron sharing within these states. In contrast, the $4f$ states with minority spins remain unoccupied and positioned energetically above the Fermi level. This phenomenon can be explained by the antiparallel coupling between the $4f$ states of Pr and the 3d states of Fe. This result is in agreement with that found by Trygg et al. [45] for $GdFe_{12}$ and Liu et al. [46] for $Gd(Co, Fe)_{12}B_6$.

After local calculation of magnetic moment in the non-equivalent crystallographic iron sites $(8i, 8f, 8j)$, we found that the total calculated magnetic moment is equal to 23.02 $\mu_B/f.u.$ when the local calculated magnetic moments are equal to 1.31 μ_B for the $2a$ site, -0.38 μ_B for Ti$(8i)$, and 2.53, 2.16, and 1.91 μ_B for iron sites $8i, 8j$, and $8f$, respectively. These results give $\langle \mu_{Fe} \rangle = 2.12$ μ_B. These values align remarkably well with the values deduced from the weighted average hyperfine field, $\langle \mu_{Fe} \rangle$, obtained by refining the Mössbauer spectra. This agreement is also reflected in the results of magnetic evaluations carried out at lower temperatures.

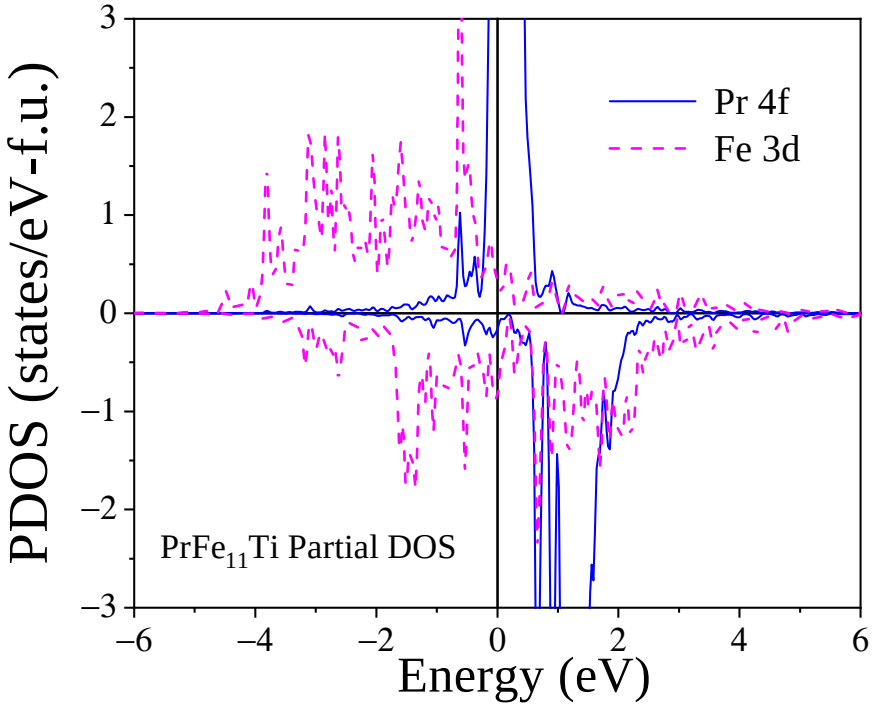

Figure 7. Partial density of states for PFT intermetallic compound.

3.4. Magnetocaloric Performance

To examine the performance of magnetocaloric materials, it is necessary to measure magnetization as a function of the magnetic field at different temperatures around T_C. We measured isothermal magnetization $M(\mu_0 H, T)$ curves in a magnetic field range of 0 to 1.55 T, as shown in Figure 8 in the Curie temperature zone. We notice that as we approach saturation and apply a small magnetic field, the magnetization at low temperature ($T < T_C$) increases significantly, meaning that our compound exhibits a ferromagnetic characteristic, whereas when the magnetic field is applied, the magnetization rises slowly above T_C, indicating that our compound is in a paramagnetic state.

The reversibility of the magnetocaloric effect is a very important criterion from an application point of view, and in this section, we use a commonly used method. Arrott plots serve as a common tool for characterizing the ferro–paramagnetic transition in magnetic materials. Through the extraction and examination of data from the $M(\mu_0 H, T)$ curves, a set of Arrott curves has been generated, as depicted in Figure 9. These curves emphasize the square of the magnetization, denoted as M^2, in relation to the ratio $\mu_0 H/M$. This approach provides a comprehensive understanding of the transition's dynamics.

Following Banerjee's criterion, a pivotal aspect in evaluating the transition's characteristics is the steepness of the straight portions near the Arrott curve at the Curie temperature T_C and elevated magnetic field ($\mu_0 H$) strengths: A negative slope of the curves indicates a first-order transition, which is characterized by abrupt transitions between ferromagnetic and paramagnetic states. A positive slope, on the other hand, suggests a second-order transition, which is characterized by more consistent and gradual shifts in magnetic characteristics as temperature or magnetic field change [47]. In the context of our sample, $PrFe_{11}Ti$ compound, analysis of the Arrott diagrams clearly shows a positive slope in the transition zone, reinforcing the hypothesis of a second-order phase transition.

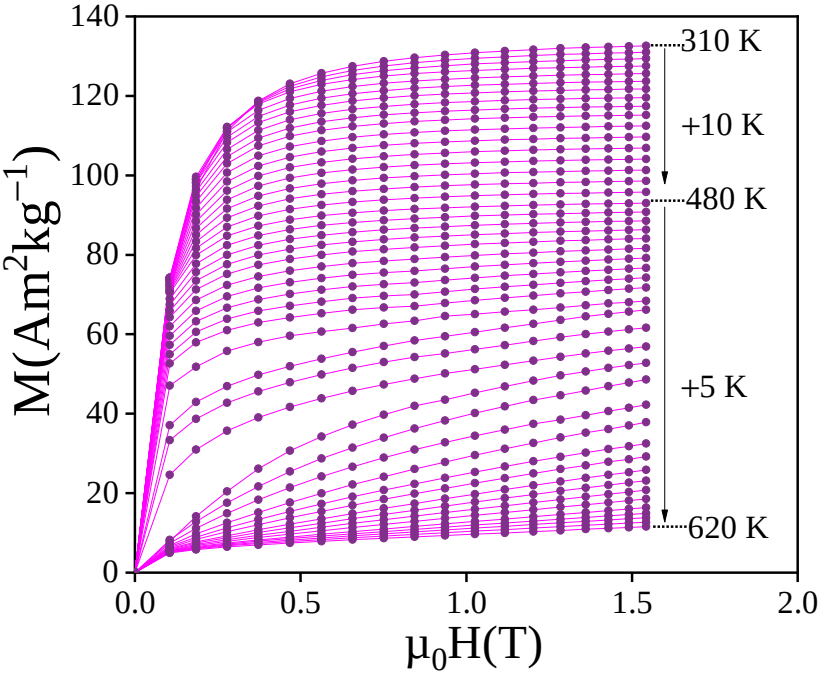

Figure 8. The isothermal magnetization curves as a function of the magnetic field. +10 K and +5 K mean the temperature step between two successive isotherms in the heating process.

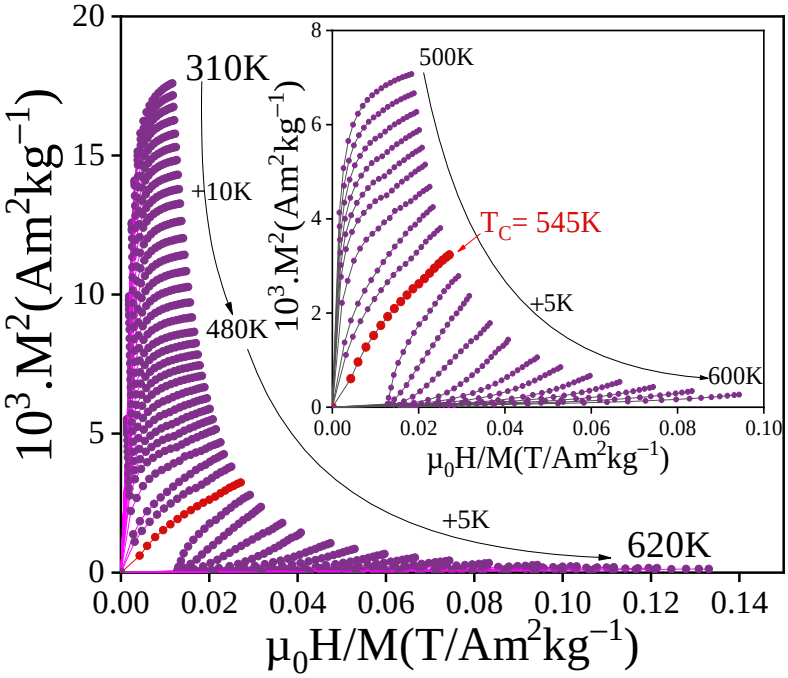

Figure 9. Arrott plots (M^2 vs. $\mu_0 H/M$) for PFT compound measured at different temperatures.

The presence of ferromagnetic ordering around room temperature and the magnetic softness of $PrFe_{11}Ti$ prompted us to assess its magnetocaloric characteristics. We used an indirect method based on magnetization isotherms as a function of the magnetic field applied for different temperatures using the Maxwell relation [48]:

$$\Delta S_M(T, \mu_0 \Delta H) = \int_0^H \mu_0 \left(\frac{\delta M}{\delta T}\right)_{P,H} dH \quad (3)$$

Table 4. Values of applied magnetic field $\mu_0\Delta H$, Curie temperature T_C, maximum of entropy variation $|-\Delta S_M^{\max}|$, relative cooling power (RCP), and the temperature-averaged entropy change parameters (TEC) of $PrFe_{11}Ti$ compared with other magnetic materials.

Sample	$\mu_0\Delta H$ (T)	T_C (K)	$-\Delta S_M^{\max}$ J/(kg·K)	RCP (J/kg)	TEC $J(K{\cdot}kg)^{-1}$	$\frac{TEC}{\mu_0\Delta H}$ $J(K{\cdot}kg{\cdot}T)^{-1}$	Ref.
$PrFe_{11}Ti$	0.5	545	1.1	23	1.1	2.2	This
	1		1.9	48	1.9	1.9	work
	1.5		2.5	70	2.44	1.6	
$GdFe_6Al_6$	2	298	0.56	25	-	-	[4]
$NdFe_{9.5}Mo_{2.5}$	5	302	2.38	-	-	-	[23]
$NdFe_{11}Ti$	1.5	552	1.5	-	-	-	[24]
$SmFe_{10}V_2$	1.5	603	1.6	-	-	-	
$GdFe_{10}Cr_2$	1.5	580	1.82	10.5	-	-	[25]
$ErFe_9Mn_3$	1	312.5	0.7	-	-	-	[26]
	5		1.92	-	-	-	

In fact, we used a computation software that relied on an integral rather than a summation to obtain the value of ΔS_M at various fields and temperatures using the equation:

$$\Delta S_M\left(\frac{T_1+T_2}{2}\right) = \frac{1}{T_1-T_2} \times \left(\int_0^{H_{\max}} M(T_2,\mu_0 H)\mu_0 dH - \int_0^{H_{\max}} M(T_1,\mu_0 H)\mu_0 dH\right) \quad (4)$$

In Figure 10, the temperature-dependent fluctuations in the magnetic entropy change of the PFT compound are presented under varying external magnetic fields. The highest ΔS_M value exhibited a consistent increase with the increasing magnetic field, reaching a magnitude of $2.4\,J{\cdot}kg^{-1}{\cdot}K^{-1}$ for a magnetic field shift from 0 to 1.5 T. The computed magnetic entropy change values for the present $PrFe_{11}Ti$ alloy surpass those reported in the literature for refrigerant materials with a $ThMn_{12}$-type structure. These comparisons are summarized in Table 4, and it is worth noting that they operate within specific temperature ranges. An essential consideration in the selection of magnetocaloric materials involves the notion of relative cooling power (RCP), a parameter introduced by Gschneidner and Pecharsky [10]. It quantifies the quantity of heat exchanged between the hot and cold sides within an ideal refrigeration cycle, offering a valuable means to evaluate the overall magnetocaloric efficiency. The calculation for this efficiency metric is as follows [16]:

$$RCP = |-\Delta S_M^{\max}| \times \delta T_{\mathrm{FWHM}} \quad (5)$$

where $-\Delta S_M^{\max}$ is the maximum of the magnetic entropy change and δT_{FWHM} is the full width at half maximum of the magnetic entropy.

It can be seen from Table 4 that the values obtained for RCP increase monotonically as the field increases, and it was found to be $75\,J{\cdot}kg^{-1}$ under an applied magnetic field of 1.5 T, while these values were quite comparable to those reported for other magnetocaloric materials.

In addition to refrigerant capacity (RCP), another crucial parameter for evaluating the suitability of materials in magnetic refrigeration technologies is the temperature-averaged entropy change (TEC). This supplementary performance metric, as introduced by L. D. Griffith et al. [49], can be determined using magnetic entropy change data in the subsequent manner:

$$TEC = \frac{1}{\Delta T_{H-C}} \max\left\{\int_{T_{mid}-\frac{\Delta T_{H-C}}{2}}^{T_{mid}+\frac{\Delta T_{H-C}}{2}} |\Delta S_M(T)| dT\right\}$$

where ΔT_{H-C} is characterized as the temperature range of the measuring device, signifying the disparity between the hot and cold heat exchangers. The temperature value denoted by T_{mid} corresponds to the midpoint of ΔT_{H-C}, which optimizes the temperature-averaged entropy change (TEC).

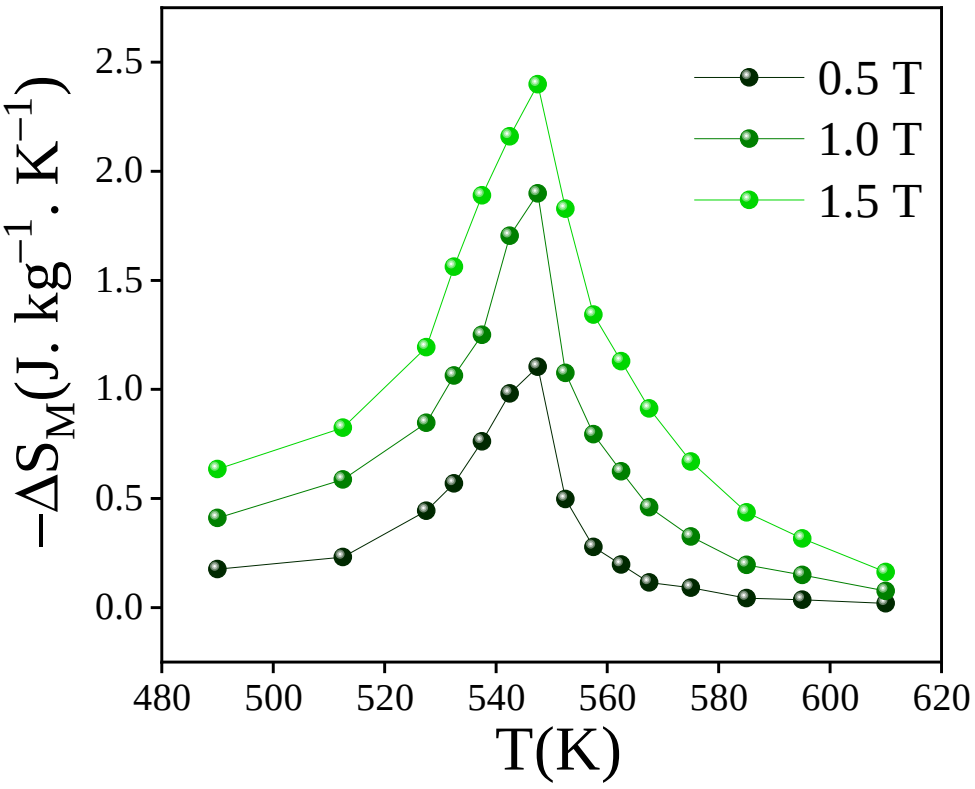

Figure 10. Magnetic entropy change vs. temperature under several magnetic fields for $PrFe_{11}Ti$ compound.

In Table 4, we provide the temperature-averaged entropy change (TEC) values for the $PrFe_{11}Ti$ compound. These values have been adjusted relative to the magnetic field strength for ease of comparison, as the TEC values reported in previous studies do not correspond to the same magnetic field strength. Based on these results, our compound demonstrates a normalized TEC ($\frac{TEC}{\Delta\mu_0 H}$) that is comparable to that of $Pr_{1.64}Sm_{0.36}Fe_{17}$ ($\frac{TEC}{\Delta\mu_0 H} = 1.24$ J(K·kg·T)$^{-1}$) [21], approximately three times higher than that of $PrCo_3Cu_2$ ($\frac{TEC}{\Delta\mu_0 H} = 0.5$ J(K·kg·T)$^{-1}$) [50]. Our values are higher than those of other compounds such as $La_{0.8}Ca_{0.05}Na_{0.15}MnO_3$ ($\frac{TEC}{\Delta\mu_0 H} = 0.91$ J(K·kg·T)$^{-1}$) [51], $Pr_{0.5}Eu_{0.1}Sr_{0.4}MnO_3$ ($\frac{TEC}{\Delta\mu_0 H} = 0.89$ J(K·kg·T)$^{-1}$) [52], $TmFe_{0.7}Mn_{0.3}O_3$ ($\frac{TEC}{\Delta\mu_0 H} = 1$ J(K·kg·T)$^{-1}$) [53], and Ho_2CoMnO_6 ($\frac{TEC}{\Delta\mu_0 H} = 0.928$ J(K·kg·T)$^{-1}$) [54]. Over a wide temperature range, the investigated compound exhibits a good magnetocaloric behavior.

4. Conclusions

To sum up, our study focused on synthesizing and characterizing polycrystalline $PrFe_11Ti$ produced via the arc-melting technique. The compound exhibited a singular tetragonal crystal structure, adhering to the space group $I4/mmm$. Magnetic assessment showed a higher Curie temperature (T_C), which might be related to a larger Fe–Fe exchange interaction (J_{Fe-Fe}). The preferred place for the Ti atom has been found as 8*i*. This finding was bolstered by XRD, DFT, and additional Mössbauer spectrometry. The determined hyperfine field is closely in line with the experimental magnetic moment of iron, derived from magnetization data. The results obtained from Mössbauer spectroscopy and magnetization were strongly in agreement with ab initio calculations using the DFT formalism. Furthermore, this study embarks on a pioneering exploration of the magnetocaloric

properties of $PrFe_{11}Ti$ ternary compounds, contributing valuable insights to the field of high-performance magnetic materials at high temperatures.

Author Contributions: Conceptualization, all authors; methodology, J.H. and H.J.; software, J.H. and H.J.; formal analysis, all authors; data curation, all authors; writing—original draft preparation, J.H. and H.J.; writing—review and editing, all authors. All authors have read and agreed to the published version of the manuscript.

Funding: This research received no external funding.

Data Availability Statement: The data used to support the findings of this study are available from the corresponding author upon request.

Acknowledgments: This work was supported by the National Center for Scientific Research (CNRS), France, and by the "Ministère de l'Enseignement Supérieur et de la Recherche Scientifique" (LPA) Laboratory, University of Sfax, Tunisia.

Conflicts of Interest: The authors declare no conflict of interest.

References

1. De Mooij, D.; Buschow, K. Some novel ternary $ThMn_{12}$-type compounds. *J. Less-Common Met.* **1988**, *136*, 207–215. [CrossRef]
2. Buschow, K. Permanent magnet materials based on tetragonal rare earth compounds of the type $RFe_{12-x}M_x$ *J. Magn. Magn. Mater.* **1991**, *100*, 79–89. [CrossRef]
3. Bhandari, C.; Paudyal, D. Enhancing stability and magnetism of $ThMn_{12}$-type cerium-iron intermetallics by site substitution. *Phys. Rev. Res.* **2022**, *4*, 023012. [CrossRef]
4. Oboz, M.; Talik, E. Properties of the GdTX (T = Mn, Fe, Ni, Pd, X = Al, In) and $GdFe_6Al_6$ intermetallics. *J. Alloys Compd.* **2011**, *509*, 5441–5446. [CrossRef]
5. Gabay, A.; Cabassi, R.; Fabbrici, S.; Albertini, F.; Hadjipanayis, G. Structure and permanent magnet properties of $Zr_{1-x}R_xFe_{10}Si_2$ alloys with R = Y, La, Ce, Pr and Sm. *J. Alloys Compd.* **2016**, *683*, 271–275. [CrossRef]
6. Hadjipanayis, G.; Gabay, A.; Schönhöbel, A.; Martín-Cid, A.; Barandiaran, J.; Niarchos, D. $ThMn_{12}$-Type Alloys for Permanent Magnets. *Engineering* **2020**, *6*, 141–147. [CrossRef]
7. Makurenkova, A.; Ogawa, D.; Tozman, P.; Okamoto, S.; Nikitin, S.; Hirosawa, S.; Hono, K.; Takahashi, Y. Intrinsic hard magnetic properties of $Sm(Fe, Co)_{12-x}Ti_x$ compound with $ThMn_{12}$ structure *J. Alloys Compd.* **2021**, *861*, 158477. [CrossRef]
8. Zhang, J.; Tang, X.; Sepehri-Amin, H.; Srinithi, A.; Ohkubo, T.; Hono, K. Origin of coercivity in an anisotropic Sm (Fe, Ti, V)$_{12}$-based sintered magnet *Acta Mater.* **2021**, *217*, 117161. [CrossRef]
9. Gschneidner, K.A.; Pecharsky, V.K.; Tsokol, A.O. Recent developments in magnetocaloric materials. *Rep. Prog. Phys.* **2005**, *68*, 1479. [CrossRef]
10. Pecharsky, V.K.; Gschneidner, K.A. Magnetocaloric effect from indirect measurements: Magnetization and heat capacity. *J. Appl. Phys.* **1999**, *86*, 565–575. [CrossRef]
11. Wada, H.; Tanabe, Y. Giant magnetocaloric effect of $MnAs_{1-x}Sb_x$. *Appl. Phys. Lett.* **2001**, *79*, 3302–3304. [CrossRef]
12. Chen, Y.F.; Wang, F.; Shen, B.G.; Hu, F.X.; Sun, J.R.; Wang, G.J.; Cheng, Z.H. Magnetic properties and magnetic entropy change of $LaFe_{11.5}Si_{1.5}H_y$ interstitial compounds. *J. Phys. Condens. Matter* **2003**, *15*, L161. [CrossRef]
13. Manekar, M.; Roy, S.B. Reproducible room temperature giant magnetocaloric effect in Fe–Rh. *J. Phys. D Appl. Phys.* **2008**, *41*, 192004. [CrossRef]
14. Phan, M.H.; Yu, S.C. Review of the magnetocaloric effect in manganite materials. *J. Magn. Magn. Mater.* **2007**, *308*, 325–340. [CrossRef]
15. Guo, Z.B.; Du, Y.W.; Zhu, J.S.; Huang, H.; Ding, W.P.; Feng, D. Large magnetic entropy change in perovskite-type manganese oxides. *Phys. Rev. Lett.* **1997**, *78*, 1142–1145. [CrossRef]
16. Gharbi, S.; Marouani, Y.; Issaoui, F.; Dhahri, E.; Hlil, E.K.; Barille, R.; Costa, B.F.O. Assessment of structural, optical, magnetic, magnetocaloric properties and critical phenomena of $La_{0.57}Nd_{0.1}Sr_{0.18}Ag_{0.15}MnO_3$ system at room temperature. *J. Mater. Sci. Mater. Electron.* **2020**, *31*, 11983–11996. [CrossRef]
17. Mandal, K.; Yan, A.; Kerschl, P.; Handstein, A.; Gutfleisch, O.; Müller, K. The study of magnetocaloric effect in R_2Fe_{17} (R = Y, Pr) alloys. *J. Phys. D Appl. Phys.* **2004**, *37*, 2628–2631. [CrossRef]
18. Chen, H.; Zhang, Y.; Han, J.; Du, H.; Wang, C.; Yang, Y. Magnetocaloric effect in R_2Fe_{17} (R = Sm, Gd, Tb, Dy, Er). *J. Magn. Magn. Mater.* **2008**, *320*, 1382–1384. [CrossRef]
19. Alvarez, P.; Gorria, P.; Sanchez-Llamazares, J.; Perez, M.J.; Franco, V.; Reiffers, M.; Curlik, I.; Gazo, E.; Kovac, J.; Blanco, J.A. Magnetic properties and magneto-caloric effect in pseudo-binary intermetallic (Ce, R)$_2Fe_{17}$ compounds (R = Y, Pr and Dy). *Intermetallics* **2011**, *19*, 982–987. [CrossRef]
20. Bouzidi, W.; Nouri, K.; Bartoli, T.; Sedek, R.; Lassri, H.; Moscovici, J.; Bessais, L. Study of the magnetic and magnetocaloric properties at low-field in $Nd_2Fe_{17-x}Si_x$ intermetallics. *J. Magn. Magn. Mater.* **2020**, *497*, 166018. [CrossRef]

21. Jaballah, H.; Bouzidi, W.; Fersi, R.; Mliki, N.; Bessais, L. Structural, magnetic and magnetocaloric properties of (Pr, Sm)$_2$Fe$_{17}$ compound at room temperature. *J. Phys. Chem. Solids* **2022**, *161*, 110438. [CrossRef]
22. Horcheni, J.; Nouri, K.; Dhahri, E.; Bessais, L. Crystal structure, critical phenomena and magnetocaloric properties of Ni-substituted ferromagnetic Pr_2Fe_{17} intermetallic compound around room temperature. *Solid State Chem.* **2023**, *326*, 124219. [CrossRef]
23. Xia, Y.; Du, H.; Xu, J.; Zhang, Y.; Wang, C.; Han, J.; Liu, S.; Xu, Q.; Yang, J. The magnetic and magnetocaloric properties of $NdFe_{12-x}Mo_x$ compounds *J. Appl. Phys.* **2012**, *111*, 07A949;.: 10.1063/1.3680204. [CrossRef]
24. Bouzidi, W.; Bartoli, T.; Sedek, R.; Bouzidi, A.; Moscovici, J.; Bessais, L. Low-field magnetocaloric effect of $NdFe_{11}Ti$ and $SmFe_{10}V_2$ compounds. *J. Mater. Sci. Mater. Electron.* **2021**, *32*, 10579–10586. [CrossRef]
25. Saidi, M.; Walha, S.; Hlil, E.; Bessais, L.; Jemmali, M. Effect of chromium substitution on structural, magnetic and magnetocaloric properties of $GdFe_{12-x}Cr_x$ intermetallic compounds, Mössbauer spectrometry and ab initio calculations. *J. Solid State Chem.* **2021**, *297*, 122019. [CrossRef]
26. Gao, P.; Xia, Y.; Gong, J.; Ju, X. Structure and Magnetic Properties of $ErFe_xMn_{12-x}$ ($7.0 \leq x \leq 9.0$, $\Delta x = 0.2$). *Nanomaterials* **2022**, *12*, 1586. [CrossRef]
27. Rietveld, H. A profile refinement method for nuclear and magnetic structures. *J. Appl. Crystallogr.* **1969**, *2*, 65–71. [CrossRef]
28. Rodríguez-Carvajal, J. Recent advances in magnetic structure determination by neutron powder diffraction. *Phys. B Condens. Matter.* **1993**, *192*, 55–69. [CrossRef]
29. Bessais, L.; Djega-Mariadassou, C. Structure and Magnetic Properties of Nanocrystalline $Sm(Fe_{1-x}Co_x)_{11}Ti$ ($x < 2$). *Phys. Rev. B* **2001**, *63*, 054412.
30. Piquer, C.; Grandjean, F.; Isnard, O.; Pop, V.; Long, G.J. A magnetic and Mössbauer spectral study of $PrFe_{11}Ti$ and $PrFe_{11}TiH$. *J. Alloys Compd.* **2004**, *377*, 1–7. [CrossRef]
31. Givord, D.; Laforest, J.; Schweizer, J.; Tasset, F. Temperature dependence of the samarium magnetic form factor in $SmCo_5$. *J. Appl. Phys.* **1979**, *50*, 2008–2010. [CrossRef]
32. Margarian, A.; Dunlop, J.; Day, R.; Kalceff, W. Phase equilibria in the Fe-rich corner of the Nd-Fe-Ti ternary alloy system at 1100 °C. *J. Appl. Phys.* **1994**, *76*, 6153–6155. [CrossRef]
33. Liu, Z.y.; Jin, Z.p.; Xia, C.s. 873 K isothermal section of phase diagram for Y-Fe-Ti ternary system. *Scr. Mater.* **1997**, *37*, 1129-1134. [CrossRef]
34. Tang, S.; Yang, C.; Wang, B.; Jin, X.; Zhang, S.; Du, Y. Structure and magnetic properties of $PrFe_{11.5-x}V_xTi_{0.5}$ compounds and their nitrides. *J. Magn. Magn. Mater.* **1998**, *189*, 341–345. [CrossRef]
35. Tang, S.; Yin, J.; Jin, Z.; Zhang, J.; Zhang, S.; Du, Y. Structure and magnetic properties of $PrFe_{10}V_xMo_{2-x}$ compounds and their nitrides. *J. Appl. Phys.* **1999**, *85*, 4687–4689. [CrossRef]
36. Tereshina, I.; Gaczyński, P.; Rusakov, V.; Drulis, H.; Nikitin, S.; Suski, W.; Tristan, N.; Palewski, T. Magnetic anisotropy and Mössbauer effect studies of $PrFe_{11}Ti$ and $PrFe_{11}TiH$. *J. Phys. Condens. Matter* **2001**, *13*, 8161. [CrossRef]
37. Kim, H.T.; Kim, Y.B.; Kim, C.S.; Jin, H. Magnetocrystalline anisotropy of $(Sm_{0.5}RE_{0.5})Fe_{11}Ti$ compounds (RE = Ce, Pr, Nd, Sm, Gd and Tb). *J. Magn. Magn. Mater.* **1996**, *152*, 387–390. [CrossRef]
38. Néel, L. Relation entre la constante d'anisotropie et la loi d'approche à la saturation des ferromagnétiques. *J. Phys. Radium* **1948**, *9*, 193–199. [CrossRef]
39. Denissen, C.; Coehoorn, R.; Buschow, K. 57 Fe Mössbauer study of $RFe_{12-x}T_x$ compounds (T= V, Cr, Mo). *J. Magn. Magn. Mater.* **1990**, *87*, 51–56. [CrossRef]
40. Blaha, P.; Schwarz, K.; Sorantin, P.; Trickey, S. Full-potential, linearized augmented plane wave programs for crystalline systems. *Comput. Phys. Commun.* **1990**, *59*, 399–415. [CrossRef]
41. Kohn, W.; Sham, L.J. Self-consistent equations including exchange and correlation effects. *Phys. Rev.* **1965**, *140*, A1133. [CrossRef]
42. Blaha, P.; Schwarz, K.; Tran, F.; Laskowski, R.; Madsen, G.K.; Marks, L.D. WIEN2k: An APW+ lo program for calculating the properties of solids. *J. Chem. Phys.* **2020**, *152*, 074101. [CrossRef] [PubMed]
43. Perdew, J.P.; Burke, K.; Ernzerhof, M. Generalized gradient approximation made simple. *Phys. Rev. lett.* **1996**, *77*, 3865. [CrossRef] [PubMed]
44. Gunnarsson, A. The Stoner model in the spin-density-functional formalism. *Phys. B C* **1977**, *91*, 329–336. [CrossRef]
45. Trygg, J.; Johansson, B.; Brooks, M.S.S. Ab initio calculation of the magnetism in $GdFe_{12}$. *J. Magn. Magn. Mater.* **1992**, *104*, 1447. [CrossRef]
46. Liu, X.B.; Altounian, Z.; Ryan, D.H. Magnetocrystalline anisotropy in Gd(Co, Fe) $_{12}B_6$: A first-principles study. *J. Alloys Compd.* **2016**, *688*, 118–122. [CrossRef]
47. Banerjee, B.K. On a generalised approach to first and second order magnetic transitions. *Phys. Lett.* **1964**, *12*, 16–17. [CrossRef]
48. Zhong, W.; Chen, W.; Ding, W.P.; Zhang, N.; Hu, A.; Du, Y.W.; Yan, Q.J. Structure, composition and magnetocaloric properties in polycrystalline $La_{1-x}A_xMnO$ (A = Na, K). *J. Eur. Phys. B* **1998**, *3*, 169–174. [CrossRef]
49. Griffith, L.D.; Mudryk, Y.; Slaughter, J.; Pecharsky, V.K. Material-based figure of merit for caloric materials. *J. Appl. Phys.* **2018**, *123*, 034902. [CrossRef]
50. Jaballah, H.; Charbonnier, V.; Bessais, L.; Mliki, N. Investigation of spin reorientation and magnetocaloric behavior in $PrCo_{5-x}Cu_x$ compounds. *Mater. Res. Bull.* **2023**, *165*, 112326. [CrossRef]

51. Choura-Maatar, S.; Nofal, M.M.; Mnassri, R.; Koubaa, W.C.; Boudjada, N.C.; Cheikhrouhou, A. Enhancement of the magnetic and magnetocaloric properties by Na substitution for Ca of $La_{0.8}Ca_{0.2}MnO_3$ manganite prepared via the Pechini-type sol-gel process. *J. Mater. Sci. Mater. Electron.* **2020**, *31*, 1634–1645. [CrossRef]
52. Sakka, A.; Mnassri, R.; Nofal, M.; Mahjoub, S.; Koubaa, W.C.; Boudjada, N.C.; Oumezzine, M.; Cheikhrouhou, A. Structure, magnetic and field dependence of magnetocaloric properties of $Pr_{0.5}RE_{0.1}Sr_{0.4}MnO_3$ (RE= Eu and Er). *J. Magn. Magn. Mater.* **2020**, *514*, 167158. [CrossRef]
53. Su, L.; Zhang, X.; Dong, Q.; Li, H.T.Y.S.H.; Cheng, Z.H. Evolution of structural, magnetic and magnetocaloric effect in $TmFe_{1-x}Mn_xO_3$ ($x \leq 0.3$) *Ceram. Int.* **2021**, *47*, 18286–18294. [CrossRef]
54. Mazumdar, D.; Das, I. Role of 3d–4f exchange interaction and local anti-site defects in the magnetic and magnetocaloric properties of double perovskite Ho_2CoMnO_6 compound *J. Appl. Phys.* **2021**, *129*, 063901. [CrossRef]